Electromagnetic Characteristic Analysis of Bidirectional Improved Flux Switching Linear-Rotary Motor

Kaikai Guo, *Member, IEEE,* and Youguang Guo, *Senior Member, IEEE*

***Abstract*— Flux concentrated structure is adopted in the design of bidirectional flux switching linear-rotary motor, which not only brings high torque/thrust density, but also increases stator iron material magnetic saturation. In order to decrease the magnetic maturation level of the motor, the stator pole width, stator pole axial length, permanent magnet (PM) width, PM axial length and stator yoke height are selected as the analysis variables, which are closely related to the two magnetic saturation regions of the stator section based on the initial analysis. The expressions of flux density in the two magnetically saturated regions of the stator core related with the selected five structure variables are derived by numerical fitting method based on the initial simulation result calculated by finite element method. Then the optimization structure variable values are achieved, a prototype and its test experiment are carried out, which verifies that the torque and thrust densities are improved and the numerical fitting method is efficient and accurate for magnetic saturation calculation.**

***Index Terms*—flux concentrated; finite element method; bidirectional flux switching linear rotary machine**

I. INTRODUCTION

THE torque and thrust density can be improved by the design of flux concentrated (FC) structure, which has been widely used in the machine design. Many different motor topologies are proposed in [1-8]. The force density, efficiency and power factor of a linear vernier machine were improved with V-shaped FC consequent pole [1]. FC permanent magnet (PM) synchronous machines with ferrite PMs were investigated by finite element method (FEM) [2][3]. The optimization design of an FC structure transverse flux machine (TFM) was conducted by Taguchi and genetic algorithm methods in [4][5], respectively. An E-core TFM with FC ferrite PMs and pole windings was presented, and its PM utilization and torque density were improved in [6]. The air-gap flux density of a doubly salient linear PM machine was improved thanks to the V-shape FC PM arrays in [7]. The flux density radial and tangential components of a coaxial magnetic gear with an FC rotor were studied by the 2-D space harmonic analysis method in [8]. Linear rotary motor (LRM) can be widely used in many fields, such as robots, screwing machines and drilling machines. The improvement of the torque/thrust density of LRM is still worth studying deeply, which has attract many scholars' attentions. The topologies, coupling effect, optimization design and decoupling control algorithm of many 2-DOF LRMs were introduced in [9]. The electromagnetic analysis of three different PM type LRMs including independent magnetic circuit LRM, flux reversal LRM, HTS LRM were calculated in [10-12].The design of a decoupled LRM was introduced based on magnetic circuit FEM, and the linear and rotary motions were achieved independently by a two proportional-integral-derivation controllers [13]. A multiphase magnetically levitated LRM was investigated and the control model was defined by the space vector model approach [14].

The bidirectional improved flux switching structure is adopted in the proposed motor, which can has FC effect whether it is in linear and rotary motions. Then the flux density of the motor is improved and the magnetic saturation of ferromagnetic material also becomes the key element to limit the torque and thrust density. In order to avoid the magnetic saturation and improve torque/thrust density, the electromagnetic characteristics of bidirectional flux switching (BFS) LRM are analyzed, the NdFeB/ferrite PM materials are selected according to the FC characteristic analysis, and the expressions of flux density in the two magnetically saturated regions of the stator section are derived by numerical fitting method based on the initial simulation results analyzed by FEM, which are related with PM circumferential and axial widths, stator pole circumferential and axial widths, and stator yoke height. Then the optimum values of electromagnetic and structure variables are obtained, a prototype is made and its test platform is set up.

II. TOPOLOGY OF BFSLRM

Fig. 1 illustrates the topology of BFSLRM. The stator section consists three independent stator units. The main feature is that the magnetized directions of the PM material embedded in the stator pole and U-shaped PM material embedded in the stator pole and stator yoke can form dual levels flux switching structure in the stator sections, and the magnetization directions of PMs arrayed in the same position in adjacent stator units are opposite. The mover salient poles are interlaced one mover pole pitch in the circumferential and axial directions, which has FC effect whether it works in linear or rotary motion. Fig. 2 illustrates the FC structure of BFSLRM. The PM material embedded in the stator pole and U-shape PM material are the

This work was supported by the High-level Talent Introduction Foundation of AUST under Grant 12365, the National Natural Science Foundation of China under Grant 51905003, Natural Science Foundation of Anhui Province under Grant 1908085QE207, China Postdoctoral Science Foundation under Grant 2019M652161 and Young Teacher Natural Science Foundation of AUST under Grant QN2018107. *(Corresponding author: Kaikai Guo.)*

Kaikai Guo is with the School of Electrical and Information Engineering & School of Mechanical Engineering, Anhui University of Science and Technology, Huainan, 232001, China (e-mail: guokai0072000@gmail.com).

Youguang Guo is with School of Electrical and Data Engineering, University of Technology Sydney, Sydney, NSW, 2007, Australia (e-mail: Youguang.guo-1@uts.edu.au).

main and auxiliary magnetomotive force sources of the main magnetic circuit, respectively. The BFC structure can enhance the reliability of the machine and improve the air gap flux density.

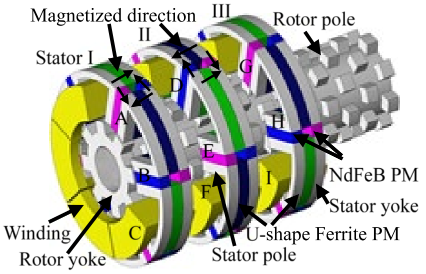

Fig. 1. The topology of BFSLRM.

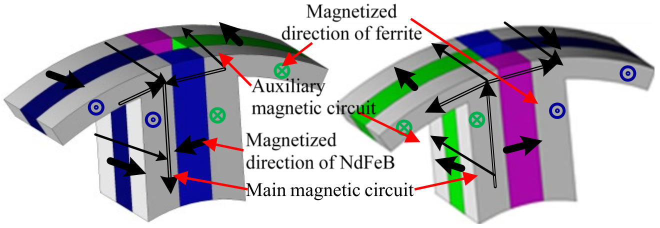

Fig. 2. The stator magnetic circuit of BFSLRM

III. FLUX CONCENTRATION ANALYSIS

A. Magnetic Saturation Analysis

Fig. 3 illustrates the flux density distributions of BFSLRM. It is noticed that the flux concentrations in positions (A, B) of the stator section are obvious. The stator inner radius (R_{si}) and the initial stator pole height (h_{sp}) are 24 mm and 20 mm, respectively. When the stator saturation area is less than 5%, the magnetic saturation of ferromagnetic material has little influence on the performance of the motor, then the maximum values of the flux densities in positions (A, B) are less than 2.1 T at the position when the radial dimensions are 26 mm and 45 mm as shown in Fig. 2, respectively, and then the material can be taken as unsaturated. Namely, $R_{si} + h_{sp}/20 *2=26$ mm; $R_{si} + h_{sp}+1$ mm= 45 mm.

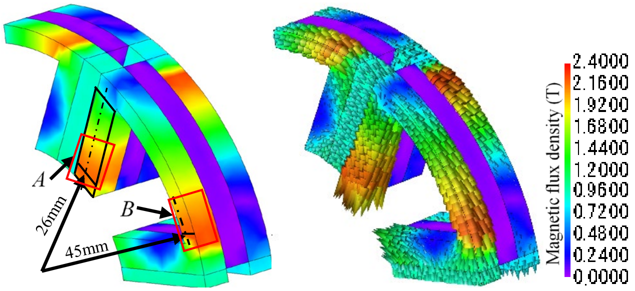

(a) (b)

Fig. 3. Flux distribution of BFSLRM, (a) magnetic contour plot, and (b) magnetic vector plot.

B. Calculation of Flux Concentration

Fig. 4 illustrates the magnetic field distribution of a single stator pole. Compared with the flux densities at positions a, b and c, it is noticed that the FC effect in position c is obvious, which is also the cause of the stator local saturation. In Fig. 4(a), $w_{s\theta}$, w_{sz}, $w_{pm\theta}$ and w_{pmz} are the circumferential and axial stator pole widths, PM pole widths, respectively. h_{sy} is the stator yoke height. $w_{s\theta}$, w_{sz}, $w_{pm\theta}$, w_{pmz} and h_{sy} are selected as the analysis parameters. The selected parameter contains the basic value and changing value. The basic values of the selected variables are 3 mm. Table I lists the initial values of the selected parameters.

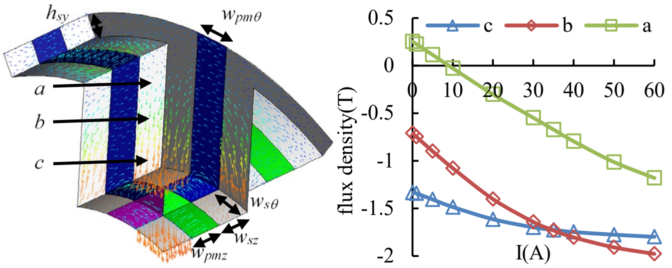

(a) (b)

Fig. 4. Magnetic flux density, (a) magnetic field distribution of single stator pole, and (b) flux densities with different currents.

TABLE I
INITIAL VALUES

Variable	Basic value	Fixed variables				
		$w_{pm\theta}$	$w_{s\theta}$	h_{sy}	w_{sz}	w_{pmz}
$w_{pm\theta}$ (mm)	3	/	5.25	3.5	5.5	5.5
$w_{s\theta}$ (mm)	3	2.75	/	3.5	5.5	5.5
h_{sy} (mm)	3	2.75	5.25	/	5.5	5.5
w_{sz} (mm)	3	2.75	5.25	3.5	/	5.5
w_{pmz} (mm)	3	2.75	5.25	3.5	5.5	/

Fig. 5(a) describes the air-gap flux density waveforms of the topology without mover slots and with mover slots. It is seen that the FC effect of the topology without mover slots is more obvious than that of the topology with mover slots. The PM embedded in the stator tooth and U-shape PM material can be taken as the main PM and auxiliary PM, respectively.

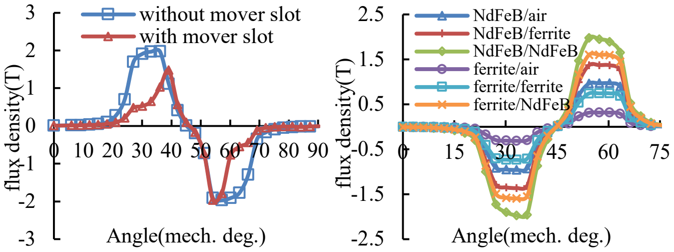

(a) (b)

Fig. 5. Air-gap flux density waveforms, (a) comparison between without mover slot and with mover slot, and (b) with different PM material combinations.

Fig. 5(b) describes the air-gap flux density waveforms when the main and auxiliary PM materials are NdFeB/air, NdFeB/ferrite, NdFeB/NdFeB, ferrite/air, ferrite/ferrite, and ferrite/NdFeB, respectively. It is noticed that the average flux density values of the six combinations are 0.95 T, 1.35 T, 1.89 T, 0.31 T, 0.73 T and 1.57 T, respectively. Although the flux densities of NdFeB/NdFeB and ferrite/NdFeB are larger than the results of NdFeB/ferrite, the torque densities of

NdFeB/NdFeB and ferrite/NdFeB are lower than that of NdFeB/ferrite when the stator saturation is considered, so the PM combined form of NdFeB/ferrite materials are taken as the PM materials when the load condition is considered. Fig. 6 illustrates the magnetic flux density waveforms with the selected five structure parameters at positions *A* and *B* when the current is 8 A. The flux density of the stator pole is analyzed by the numerical fitting method.

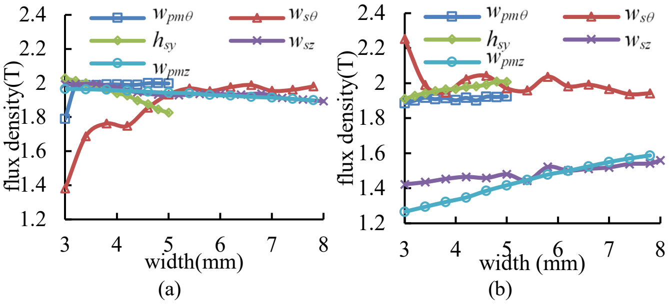

(a) (b)

Fig. 6. Magnetic flux density waveforms with the selected five structure parameters when the current is 8 A, (a) position *A*, and (b) position *B*.

The expressions of flux density in the ferromagnetic material are

$$B_1(x,n)=B_1(a_0,a_k,b_k,w,x,n)=a_0+\sum_{k=1}^{n}a_k\cos kwx+b_k\sin kwx \quad (1)$$

$$B_2(x,n)=B_2(p_1,p_2,p_3,p_4,\ldots x,n)=p_1x+p_2x^2+p_3x^3+\ldots \quad (2)$$

According to Table I, Fig. 6, (1) and (2), the expressions of flux density at positions *A* and *B* in the stator section related with the selected five variables are

$$\begin{aligned}B_{\mathrm{A}}=k_{\mathrm{A}}\cdot B_{1\_w_{pm\theta}}(w_{pm\theta},n_{A\_w_{pm\theta}})B_{1\_w_{s\theta}}(w_{s\theta},n_{A\_w_{s\theta}})\\ B_{2\_h_{sy}}(h_{sy},n_{A\_h_{sy}})B_{1\_w_{sz}}(w_{sz},n_{A\_w_{sz}})B_{2\_w_{pmz}}(w_{pmz},n_{A\_w_{pmz}})\end{aligned} \quad (3)$$

$$\begin{aligned}B_{B}=k_{\mathrm{B}}\cdot B_{2\_w_{pm\theta}}(w_{pm\theta},n_{B\_w_{pm\theta}})B_{2\_w_{s\theta}}(w_{s\theta},n_{B\_w_{s\theta}})\\ B_{2\_h_{sy}}(h_{sy},n_{B\_h_{sy}})B_{2\_w_{sz}}(w_{sz},n_{B\_w_{sz}})B_{2\_w_{pmz}}(w_{pmz},n_{B\_w_{pmz}})\end{aligned} \quad (4)$$

where,

$$\begin{aligned}k_{\mathrm{A}}=(B_{1\_w_{pm\theta}}(2.75,n_{A\_w_{pm\theta}})B_{1\_w_{s\theta}}(8.25,n_{A\_w_{s\theta}})B_{2\_h_{sy}}(3.5,n_{A\_h_{sy}})\\ B_{1\_w_{sz}}(5.5,n_{A\_w_{sz}})B_{2\_w_{pmz}}(5.5,n_{A\_w_{pmz}}))^{-4}\end{aligned}$$

$$\begin{aligned}k_{\mathrm{B}}=(B_{2\_w_{pm\theta}}(2.75,n_{B\_w_{pm\theta}})B_{2\_w_{s\theta}}(8.25,n_{B\_w_{s\theta}})B_{2\_h_{sy}}(3.5,n_{B\_h_{sy}})\\ B_{2\_w_{sz}}(5.5,n_{B\_w_{sz}})B_{2\_w_{pmz}}(5.5,n_{B\_w_{pmz}}))^{-4}\end{aligned}$$

C. Calculation of Air-gap Flux Density

Taking cogging torque and detent force as analyzed objectives, the optimization design is calculated by 3-D FEM, and multiple sets of structural parameters are achieved. Table II are the main structural parameters of three different topologies, which are obtained without considering magnetic saturation. According to (3) and (4), the flux density in the positions *A* and *B* can be calculated. Fig. 7 illustrates the basic model of stator I and air-gap flux density waveforms of the three topologies. It is noticed that the average values of the air-gap flux density corresponding to the stator pole are 1.25 T, 1.13 T and 1.2 T, respectively.

TABLE II
MAIN STRUCTURAL PARAMETERS OF BFSLRM

	Parameters (mm)					B_A (T)	B_B (T)
	$W_{PM\theta}$	$w_{s\theta}$	h_{sy}	w_{sz}	w_{pmz}		
Topology I	5.5	5.5	5	5.5	5.5	1.57	1.65
Topology II	4	5.5	5	7.5625	5.5	1.54	1.54
Topology II	5.5	7.5625	5	5.5	4	1.42	1.58

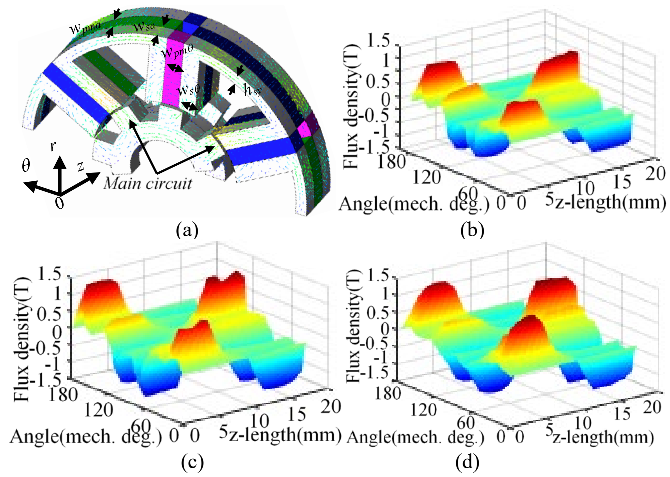

(a) (b)

(c) (d)

Fig. 7. Air-gap flux density distribution of stator I, (a) basic model, (b) topology I, (c) II, and (d) III.

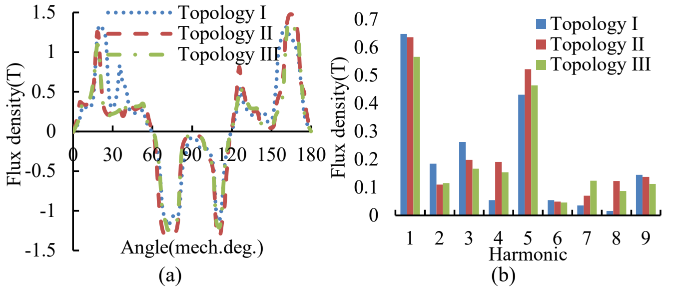

(a) (b)

Fig. 8. Air-gap magnetic flux density distributions of topology I, II and III, (a) waveforms, and (b) main harmonics.

TABLE III
MAIN STRUCTURAL VARIABLES OF TOPOLOGY I

Parameters	Value	Parameters	Value
Outer stator radius (mm)	47	Inner stator radius (mm)	24
Stator yoke height (mm)	3.5	Stator pole pitch(mm, z)	35.7
Mover diameter (mm)	23.4	Mover pole height (mm)	5.8
PM width (mm, *θ*)	5.5	PM with (mm, z)	5.5
Mover pole width (mm, *θ*)	7.6	Stator pole width (mm, *θ*)	16.5
Stator pole width (mm, *z*)	6	Stator pole width (mm, *z*)	16.5

Fig. 8 illustrates the air-gap flux density in the middle of the stator ferromagnetic pole region and harmonic analysis results. It is seen that the fundamental values of the air-gap flux density waveform of the three topologies are 0.65 T, 0.63 T and 0.565 T, respectively. According to Figs. 7 and 8, topology I has the highest air-gap flux density, which is selected as the analysis object. Table III lists the main structural variables of topology I. Fig. 9 (a) shows the air-gap flux density waveforms of topology I. It is seen that the average values of the air gap flux density in the maximum value region is 1.54 T.

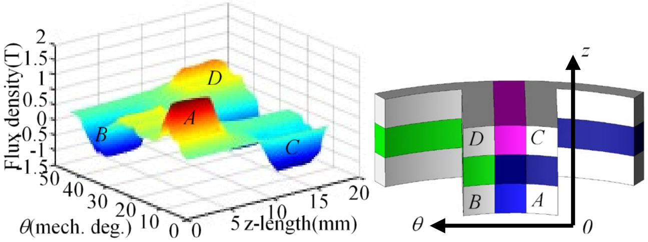

(a) (b)

Fig. 9. Air-gap flux density waveform of the single stator pole region at no load condition, (a) air-gap flux density, and (b) single stator pole region.

IV. EXPERIMENTAL VERIFICATION

The prototype and experimental platform of BFSLRM are shown in Fig. 10. Table IV lists the main specifications of the prototype.

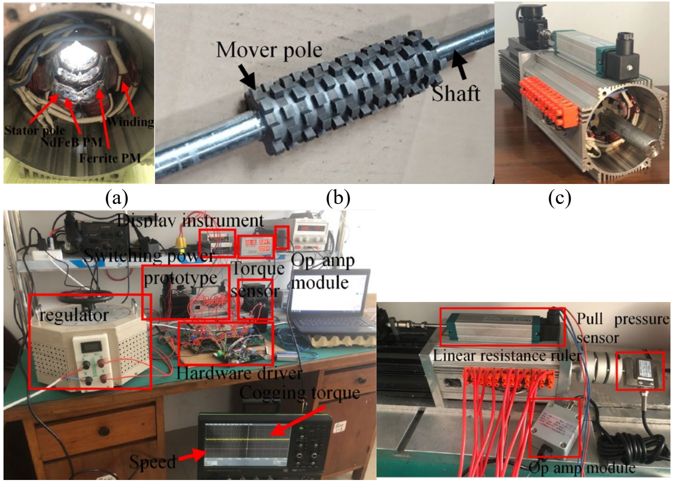

(a) (b) (c)

(d) (e)

Fig. 10. Prototype of BFSLRM: (a) stator section, (b) mover section, (c) the prototype of BFSLRM, (d) testing platform of rotary motion, and (e) testing platform of linear motion.

TABLE IV
SPECIFICATION OF THE PROTOTYPE

Parameters	Value	Parameters	Value
Rated power (W)	200	Rated voltage (V)	30
Rated current (A)	10	Rated frequency (Hz)	80
Stator resistance (Ω)	5.5	Rated speed (r/min)	1200
Axial stroke (mm)	44	Mover weight (kg)	1.701
Stator inductance (mH)	16.5	Stator winding number (turns)	90

The test bench of BFSLRM consists of the prototype, hardware driver, torque and speed sensor, pull pressure sensor and oscilloscope. The hardware driver contains the DSP controller, data collecting module, and drive module. The DSP controller can mainly complete signal processing, algorithmic calculations and communicate with the host computer. The data collecting module mainly includes the sample of the current signals from the current sensor (CSM006NPT3.3), the voltage signals from the voltage sensor (VSM025A), axial position signal from linear resistance ruler (BW-75 mm), and the rotary speed signal from the resolver (TS2540N321E64). The drive module containsighteen metal-oxide-semiconductor field-effect transistors (IRFP 460) and optocoupler device (TLP250).

Fig. 11 shows the winding arrangements of rotary and linear motions. The homonymous end of phases *D*, *E* and *F* is different when BFSLRM works in rotational or rectilinear motion. Fig. 12 illustrates the back EMF waveforms when the motor is in rotational or rectilinear motion. Since there are some manufacturing errors in the prototype, the magnetic flux leakage is increased, and the amplitude of back EMF measured by the experiment is slightly less than simulation result.

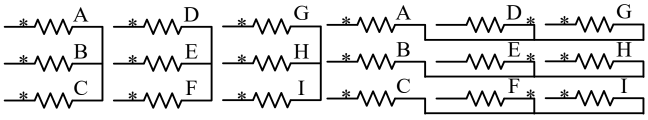

(a) (b)

Fig. 11. Winding arrangement, (a) rotation, and (b) linear motion

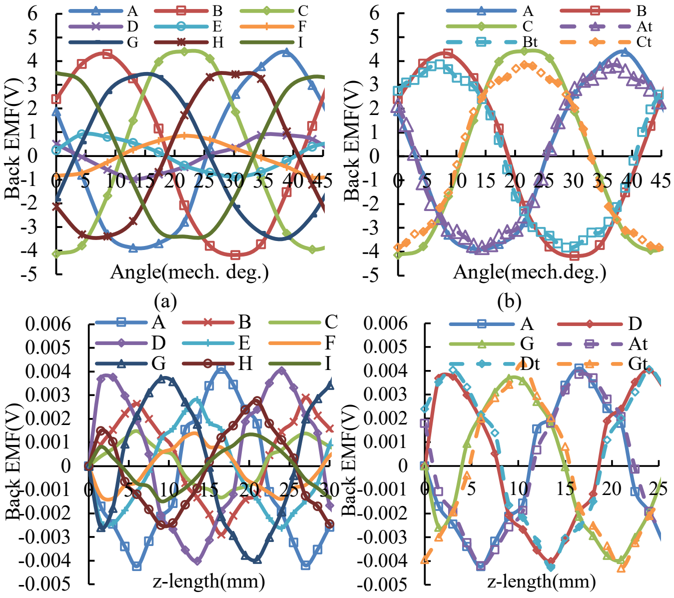

(a) (b)

(c) (d)

Fig. 12. Back EMF waveforms, (a) simulation result of rotary motion, (b) test result of rotary motion, (c) simulation result of linear motion, and (d) test result of linear motion.

Fig. 13 shows the ripples and maximum values of cogging torque and detent force when the mover is in different positions. The ripple and maximum values are different, but the changing trend is similar. Fig. 14 illustrates the torque and thrust waveforms of the motor under different currents and angles. It is noticed that when the current is 10 A, the maximum value of torque is 5.47 Nm when the initial phase angle is 130 deg., and the maximum value of thrust is 32.4 N when the initial phase angle is 120 deg. When the initial phase is less than 30 deg., the motor is hard to start.

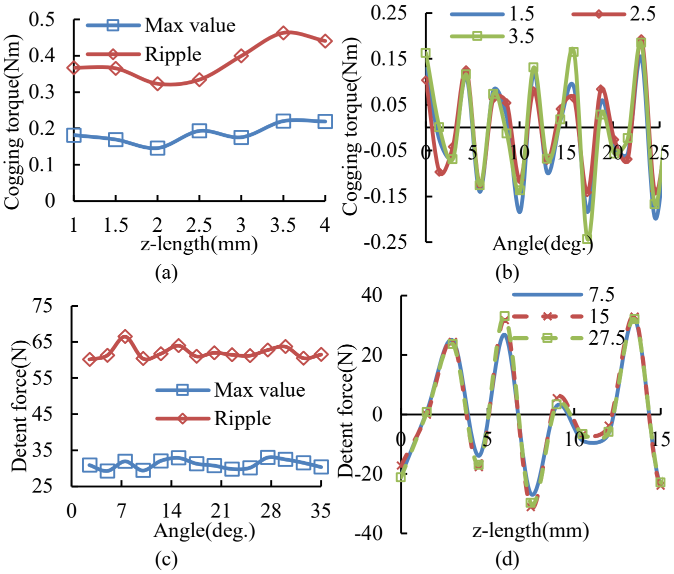

Fig. 13. Cogging torque and detent force when the mover is in different positions, (a) ripple and amplitude of cogging torque, (b) cogging torque when the mover is in different axial positions, (c) ripple and amplitude of detent force, and (d) detent force when the mover is in different circumferential positions.

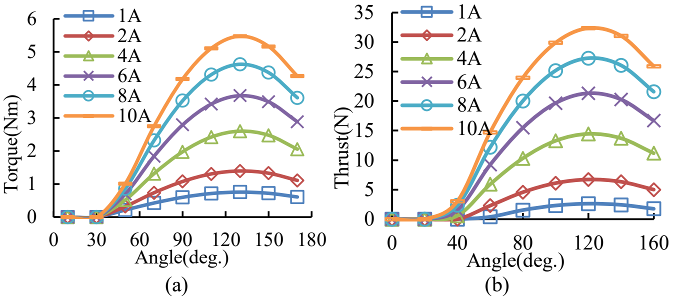

Fig. 14. Torque and thrust waveforms of the motor under different currents and angles, (a) torque, and (b) thrust force.

Fig. 15 and 16 show the cogging torque/detent force, torque/thrust waveforms analyzed by 3-D FEM and experiment test. Since the magnetic circuit of BFSLRM forms a closed loop in the circumferential direction, the machining errors of the stator pole and PM pole close to the air gap can bring larger effect on the detent force/thrust than cogging torque/torque, then the discrepancy between the simulation and test results of detent force/thrust is larger than that of cogging torque/torque. Then the measured torque and thrust values are slightly smaller than the simulation results, which are within the acceptable range. The measured torque and thrust are 5.15 Nm, 29.64N, respectively.

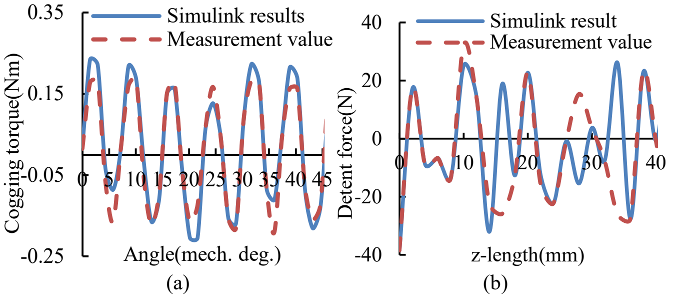

Fig. 15. Comparison of the cogging torque and detent force, (a) cogging torque, and (b) detent force.

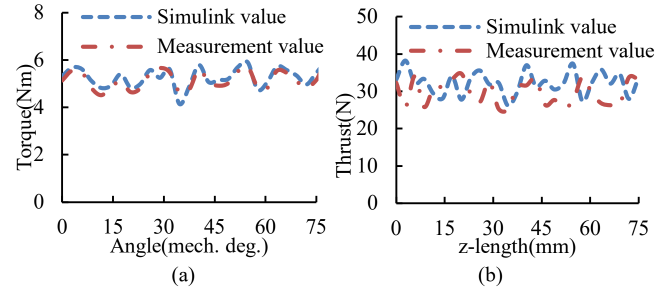

Fig. 16. Comparison of torque/thrust, (a) torque waveforms, and (b) thrust waveforms.

V. CONCLUSIONS

The rotary and linear motions of BFSLRM with the improved flux switching structure are achieved, which can improve the torque/thrust density and air gap flux density, and it also bring the magnetic saturation of ferromagnetic materials, which is the key factor to limit the torque/thrust density. In order to avoid the magnetic saturation level of stator ferromagnetic materials under the load condition, the FC effect of BFSLRM is analyzed in the paper. The NdFeB/ferrite are selected as the PM materials. The expressions of the flux densities of position *A* and *B* related with the selected five variables are derived by numerical fitting method. Then the optimization structure variables are obtained. A prototype of BFSLRM is manufactured, and its test platform is established. The electromagnetic characteristics of BFSLRM are analyzed by 3-D FEM and verified by the experiment. And it also verified that numerical fitting method is an effective method to avoid the magnetic saturation of 3-D motor.

REFERENCES

[1] A. A. Almoraya, N. J. Baker, K. J. Smith, and M. A. H. Raihan, “Design and analysis of a flux-concentrated linear vernier hybrid machine with consequent poles,” *IEEE Trans. Ind. Appl.*, vol. 55, no. 5, pp. 4595-4604, Sep. 2019.

[2] J. W. Jung, K. T. Jung, B. H. Lee, and J. P. Hong, “Design and analysis of ferrite magnet flux concentrated PMSM with cross-laminated rotor core using equivalent 2-D FEA,” *IEEE Trans. Energy Convers.*, vol. 34, no. 3, pp. 1623-1631, Sep. 2019.

[3] J. H. Park, K. T. Jung, Y. H. Jung, M. S. Lim, M. H. Yoon, J. P. Hong, and J. W. Jung, “Design and verification for the torque improvement of a concentrated flux-type synchronous motor for automotive applications,” *IEEE Trans. Ind. Appl.*, vol. 55, no. 4, pp. 3534-3543, Jul. 2019.

[4] J. Hui, M. Gao, and Y. Wang, “Design and optimization of transverse flux machine with passive rotor and flux concentrating structure,” *IET Elect. Power Appl.*, vol. 13, no. 7, pp. 922-931, Jul. 2019.

[5] B. Zhang, A. Wang, and M. Doppelbauer, “Multi-objective optimization of a transverse flux machine with claw-pole and flux-concentrating structure,” *IEEE Trans. Magn.*, vol. 52, no. 8, Aug. 2016, Art. no. 8107410.

[6] T. Husain, I. Hasan, Y. Sozer, I. Husain, and E. Muljadi, “Design of a modular E-core flux concentrating transverse flux machine,” *IEEE Trans. Ind. Appl.*, vol. 54, no. 3, pp. 2115-2128, May 2018.

[7] A. A. Almoraya, N. J. Baker, K. J. Smith, and M. A. H. Raihan, “Flux concentrated doubly salient linear permanent magnet machine,” *Journal Engin.*, vol.17, no.6, pp. 4247-4251, Jun. 2019.

[8] H. M. Shin and J. H. Chang, “Analytical magnetic field calculation of coaxial magnetic gear with flux concentrating rotor,” *IEEE Trans. Magn.*, vol. 52, no. 7, Jul. 2016, Art. no. 7004404.

[9] L. Xie, J. Si, Y. Hu, and Z. Wang, “Overview of 2-degree-of-freedom rotary-linear motors focusing on coupling effect,” *IEEE Trans. Magn*, vol. 55, no. 4, Apr. 2019, Art. no. 8200611.

[10] K. Guo, S. Fang, H. Lin, Y. Huang, Y. Zhang, and H. Yang. “A linear-rotary permanent magnet actuator with independent magnetic circuit structure,” *IEEE Trans. Appl. Supercond.*, vol. 26, no. 7, Oct. 2016, Art. no. 0611706.

[11] K. Guo and Y. Guo, “Key parameter design and analysis of flux reversal linear rotary permanent magnet actuator,” *IEEE Trans. Appl. Supercond.*, vol. 29, no. 2, Mar. 2019, Art. no. 0600405.

[12] S. Fang, K. Guo, H. Lin, D. Wang, and H. Yang, “Electromagnetic analysis of a HTS linear-rotary permanent magnet actuator,” *IEEE Trans. Appl. Supercond.*, vol. 26, no. 7, Oct. 2016, Art. no. 5208105.

[13] S. Li, K. W. E. Cheng, N. Cheung, and Y. Zou, “Design and control of a decoupled rotary-linear switched reluctance motor,” *IEEE Trans. Energy Convers*., vol. 33, no. 3, pp. 1363- 371, Sep. 2018.

[14] S. M. Miri´c, R. V. Giuffrida, D. Bortis, and J. W. Kolar, “Enhanced complex space vector modeling and control system design of multiphase magnetically levitated rotary-linear machines,” *IEEE J. Emerg. Sel. Topics Power Electron.*, vol. 8, no. 2, pp. 1833-1849, Jun. 2020.